31st Annual International Conference of the IEEE EMBS
Minneapolis, Minnesota, USA, September 2-6, 2009

An Ultra-wideband Microwave Tomography System: Preliminary Results

Colin Gilmore, Puyan Mojabi, Amer Zakaria, Majid Ostadrahimi, Cam Kaye,
Sima Noghanian, Lotfollah Shafai, Stephen Pistorius, and Joe LoVetri

***Abstract*— We describe a 2D wide-band multi-frequency microwave imaging system intended for biomedical imaging. The system is capable of collecting data from 2-10 GHz, with 24 antenna elements connected to a vector network analyzer via a 2×24 port matrix switch. Through the use of two different non-linear reconstruction schemes: the Multiplicative-Regularized Contrast Source Inversion method and an enhanced version of the Distorted Born Iterative Method, we show preliminary imaging results from dielectric phantoms where data were collected from 3-6 GHz. The early inversion results show that the system is capable of quantitatively reconstructing dielectric objects.**

I. INTRODUCTION

Microwave Tomographic (MWT) imaging is a promising alternative or complementary biomedical diagnostic technique for conventional soft-tissue imaging modalities. MWT uses microwave scattering measurements in the frequency range of a few hundred MHz up to a few GHz to quantitatively reconstruct the bulk-electrical properties, permittivity and effective conductivity of the object being imaged. Advantages of microwave tomography include (1) its low cost and portability, especially relative to MRI and x-ray CT; (2) its use of safe non-ionizing radiation; (3) its ability to image bulk-electrical properties as a feature of tissue that is not imaged by most other modalities; and (4) its ability, without the use of contrast agents, to quantitatively reconstruct frequency dependent permittivity and conductivity profiles of living tissue as a way of identifying physiological conditions of those tissues. The most studied application for biomedical MWT is for breast cancer detection, with some preliminary clinical studies completed (e.g., [1]). One possible application of MWT is in the frequent monitoring of tissue for the early detection of disease. Significant progress in microwave imaging has been made in the last decade, with experimental prototypes having been used for the imaging of excised pigs' legs [2], a canine heart, [3].

One of the major problems holding back biomedical MWT from widespread clinical acceptance is a lack of resolution. One possible way of improving the resolution is through the use of wide-band MWT systems, and in this paper, we present preliminary results from an ultra-wideband microwave tomography system, which is capable of operating from 2 GHz to 10 GHz (although our preliminary results are from 3 to 6 GHz). To the best of our knowledge, this is a significant increase in frequency range over any previously reported MWT system, e.g., [2], [4]–[6]. Our system utilizes a small number (in this paper < 5) of single frequencies to create quantitative images of the dielectric permittivity. The images are generated with one of two non-linear inversion algorithms: an enhanced version of the Distorted Born Iterative Method (DBIM), and the Multiplicative Regularized Contrast Source Inversion (MR-CSI) method. The use of non-linear inversion algorithms is necessary because linearizing assumptions about wave propagation, which allow for much simpler imaging algorithms, do not accurately model the actual physics.

In its current configuration, the ultra-wideband MWT system assumes that both imaging targets and wave-field propagation is in 2D. In this case, the E_z field is given by the scalar Helmholtz equation.

II. OVERVIEW OF SYSTEM

A photograph of the current prototype is shown in Fig.1. We have employed a two-port Agilent 8363B PNA-Series Network Analyzer (NA) as our microwave source and receiver, capable of producing measurements at discrete frequencies or sweeps within the required frequencies at an approximate system dynamic range of 120dB (an additional 15dB of dynamic range is available using the configurable test set). The NA is connected to the antennas with a 2×24 cross-bar mechanical switch (Agilent 87050A-K24), which provides excellent isolation (> 100 dB) over the frequency range of interest. Twenty-four antennas are arranged at even intervals of 15 degrees in a circular array at the midpoint height along the inside of a plastic cylinder. The cylinder has a radius of ≈ 22 cm, is 50.8 cm tall and is water-tight, allowing it to be filled with a matching liquid (not utilized in this work). For use with certain classes of test targets, there is also a motor assembly located underneath the cylinder support structure that consists of two precision stepper motors arranged to provide accurate positioning of the target within the chamber. The test target may be placed on a plastic platform mounted on a central teflon pillar protruding from a water-tight, sealed hole in the center of the cylinder's bottom boundary, and can be rotated 360° (at increments smaller than 1° if needed). A vertical movement range for the pillar of roughly 15 cm is also accommodated

Stephen Pistorius is with Medical Physics, Department of Physics and Astronomy, University of Manitoba, Winnipeg, Canada.

Sima Noghanian is with Dept. of Electrical Engineering, University of North Dakota, Grandforks, USA

All other authors are with Dept. of Electrical and Computer Engineering, University of Manitoba, Winnipeg, Canada lovetri@ee.umanitoba.ca

This work supported by NSERC, Western Economic Diversification Canada, CancerCare Manitoba and MITACS.

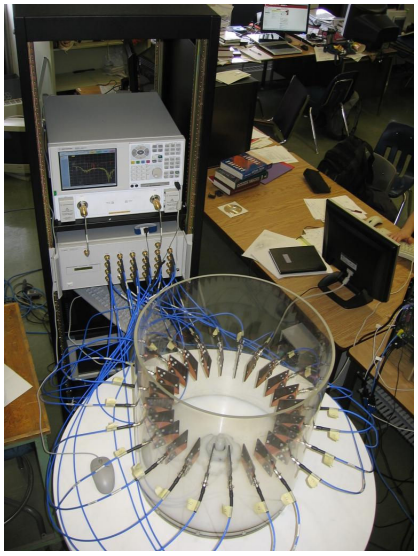

Fig. 1. The ultra-wideband microwave tomography system. The 24 Vivaldi antennas are connected to a network analyzer via a 2×24 switch.

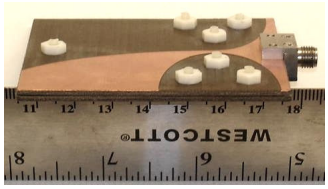

Fig. 2. Close-up of one of the double layered Vivaldi antennas used in the microwave imaging system. The two layers are held together with teflon screws.

by the motor assembly to provide full 3-D positioning of the target through the 2-D plane of the antenna array.

Communication between the NA, switch, and the controlling computer is accomplished through the General Purpose Interface Bus (GPIB), operating via a GPIB-Ethernet hub. The data acquisition process is entirely automated, and data collection is quite fast. A measurement of $23 \times 24 = 552$ data points takes less than 1 minute (this time depends highly on the sweep time utilized for the NA).

A. Antenna Description

For this system, we utilize Vivaldi antennas [7] which have been specifically designed and improved for this near field microwave imaging system [8]. Strictly defined, the bandwidth of the antennas is from 3 GHz to 10 GHz, although in practice this may be pushed to 2-10 GHz. These antennas utilize a double-layer construction which significantly reduces the cross-polarization level of radiation pattern [8]. This is critical to the use of the scalar 2D assumption about the wave propagation in the chamber, as antennas which created and detected x and y polarized fields would seriously degrade the resultant images. A picture of one of the antennas is shown in Fig. 2.

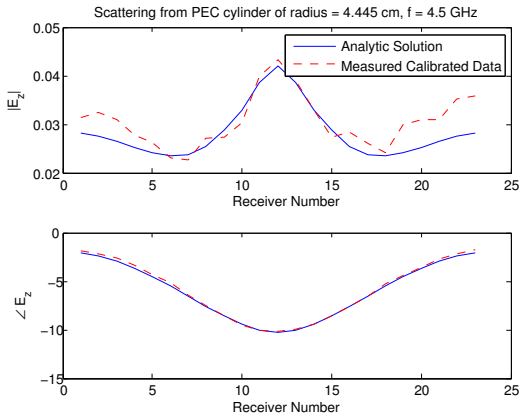

Fig. 3. Magnitude and phase comparison of scattered fields (E_z) from a PEC cylinder. The solid blue line shows the calibrated measured fields, and the analytic solution is shown with a dashed red line. The frequency was 4.5 GHz and the radius of the cylinder is 4.445 cm.

III. PROBLEM FORMULATION

Under the assumption of 2D objects and field excitation, the total electric field in the z direction satisfies the scalar Helmholtz equation. The total field may be split into incident and scattered parts: $E_z^{\text{tot}} = E_z^{\text{sct}} + E_z^{\text{inc}}$, and the scattered field can be shown to satisfy [9]

$$[\nabla^2 + k_{\text{b}}^2(\mathbf{r})]E_z^{\text{sct}}(\mathbf{r}) = -k_b^2(\mathbf{r})E_z^{\text{tot}}\chi(\mathbf{r}), \tag{1}$$

where $k_{\text{b}} = \sqrt{\omega^2\mu_0\epsilon_{\text{b}}}$ is the background wavenumber, and the electric contrast is given by

$$\chi(\mathbf{r}) = \frac{\epsilon(\mathbf{r}) - \epsilon_{\text{b}}}{\epsilon_{\text{b}}}, \tag{2}$$

where ϵ_b is the complex permittivity of the background medium. The permittivities are taken to be complex so as to allow the modeling of both polarization and conductive losses. With an assumption of an $e^{j\omega t}$ time-dependency, the complex permittivity of an object may be written as

$$\epsilon(\mathbf{r}) = \epsilon'(\mathbf{r}) + j\epsilon''(\mathbf{r}) = \epsilon'(\mathbf{r}) - j\frac{\sigma_{\text{eff}}(\mathbf{r})}{\omega} \tag{3}$$

where σ_{eff} is the effective conductivity at frequency ω.

A. Inversion Algorithms

In order to invert the data taken from this MWT system, we have implemented [10] two distinct inversion algorithms: the Multiplicative-Regularized Contrast Source Inversion method [11], [12] and an enhanced version of the Distorted Born Iterative Method (DBIM) [13] (which is equivalent to the Gauss-Newton method [10], [14]). Both algorithms formulate the mathematical inverse problem as a non-linear optimization problem which is iteratively solved for the complex permittivity of the unknown scatterer. The most significant difference between the two algorithms is that the enhanced-DBIM approach requires the repeated use of a forward solver, while the MR-CSI method does not.

Briefly, the DBIM method attempts to find the contrast which minimizes the objective function

$$F_{\mathrm{DBIM}} = \left\| \tilde{E}_z^{\mathrm{sct}} - E_z^{\mathrm{sct}} \right\|_S^2, \tag{4}$$

where $\tilde{E}_z^{\mathrm{sct}}$ is the measured scattered field, E_z^{sct} represents the predicted scattered field from the estimated contrast χ, and S denotes the measurement surface. The minimization is accomplished by approximating the function with a Taylor expansion and utilizing the Gauss-Newton optimization method. The process of regularization is critical to the success of the DBIM inversion method, and the details of the algorithm may be found in [10], [13], [14].

On the other hand, the MR-CSI method seeks to minimize the objective function

$$F_{\mathrm{CSI}} = \frac{\left\| \tilde{E}_z^{\mathrm{s}} - \mathcal{G}_{\mathrm{S}}\{w\} \right\|_S^2}{\left\| \tilde{E}_z^{\mathrm{s}} \right\|_S^2} + \frac{\left\| \chi E_z^{\mathrm{inc}} - w + \chi\, \mathcal{G}_{\mathrm{D}}\{w\} \right\|_D^2}{\sum_m \left\| \chi E_z^{\mathrm{inc}} \right\|_D^2} \tag{5}$$

where $\mathcal{G}_{\mathrm{S}}$ and $\mathcal{G}_{\mathrm{D}}$ represent Green's function operators [12], the contrast sources are given by $w(\mathbf{r}) = E_z(\mathbf{r})\chi(\mathbf{r})$, and D denotes the domain where the scatterer is located. The CSI method forms two interlaced sequences in χ and w, which are minimized by an interlaced application of the conjugate gradient method. The use of (a) the different objective function, and (b) two unknowns, allows the objective function to be minimized without any external regularization, and without calling a forward solver.

Both inversion methods are further enhanced with a multiplicative regularizer, which is left to the references [10], [11], [15]. The use of a multiplicative regularizer significantly enhances the performance of the inversion algorithms.

IV. SYSTEM CALIBRATION

To calibrate the S_{21} values measured by the NA into the field values required as input to the inversion algorithms, we first measure the scattered fields from a metallic cylinder with a known radius placed in the middle of the chamber. We denote these S parameters as S_{21}^{known}. Next, the scattering experiment is repeated, but with the unknown target present. These S parameters are denoted S_{21}^{meas}. Assuming a 2D line source, we further denote the analytic scattered fields from the known metallic cylinder as $E_z^{\mathrm{sct,known}}$. Then, the calibrated measured fields for the unknown target are calculated by

$$E_z^{\mathrm{sct,cal}} = \frac{E_z^{\mathrm{sct,known}}}{S_{21}^{\mathrm{known}}} S_{21}^{\mathrm{meas}}. \tag{6}$$

This calibration will remove any magnitude/phase errors which are common to both known and unknown measurements, including cable/connector shifts and shifts in the reference plane. An example of the analytic scattered fields and the calibrated measured fields for the scattering from a metallic cylinder of radius 4.445 cm, at a frequency of 4.5 GHz are shown in Fig. 3. The phase matches quite well, while the magnitude of the plot has some errors. This is most likely due to mutual coupling issues with the antennas.

V. PRELIMINARY RESULTS

For an initial phantom object, we utilize a circular teflon cylinder, and an approximately square wooden cylinder. We have measured the wood to have a complex relative permittivity of $\epsilon_r^{\mathrm{wood}} \approx 2.0 - j0.2$, and the teflon has been measured to have a complex relative permittivity of $\epsilon_r^{\mathrm{tefl.}} \approx 2.1 - j0.2$ (both at 3 GHz). The targets were placed in the chamber, as shown in Fig. 4 with an air background, and 23×24 measurements were taken for the frequencies of 3, 4, 5, and 6 GHz.

The single-frequency MR-CSI reconstruction at 3 GHz is shown in Fig. 5, and a simultaneous multi-frequency reconstruction from data from 3-6 GHz in 1 GHz steps is shown in Fig. 6. In the multi-frequency case, data from all frequencies are simultaneously inverted, with the data from each frequency equally weighted. The overall shape of the scatterer is clear from the 3 GHz reconstruction, although the imaginary part leaves much to be desired. In the multi-frequency reconstruction, the imaginary part of the reconstruction is better. In both reconstructions, the real part of the permittivity for the teflon cylinder is overshot. We also note that the off-axis twist to the wood in all reconstructions correctly reflects the physical orientation of the wood for the measurement.

The single-frequency 3 GHz reconstruction from the enhanced-DBIM method is shown in Fig. 7, and a frequency-hopping based reconstruction is shown in Fig. 8. With the frequency-hopping scheme, the data from each frequency are inverted independently, and the solution from the lower frequency is used as the initial guess for the next higher frequency. The DBIM is much better suited to a frequency-hopping approach than a simultaneous multi-frequency reconstruction.

Qualitatively, the DBIM 3 GHz single frequency reconstruction is quite close to the MR-CSI reconstruction. Once again, both targets are visible, with the larger errors in the imaginary part of the reconstruction. For the DBIM multi-frequency reconstruction, the edges of the targets are very clear (much clearer than the MR-CSI reconstruction). However, in the imaginary part of the reconstruction, the interiors of the objects have significant errors.

VI. CONCLUSION

We have described an ultra-wideband microwave imaging system, capable of collecting data from 2-10 GHz. For this system, we have shown successful preliminary reconstructions based on data collected from 3-6 GHz. In particular, these results illustrate the potential that ultra-wideband data collection provides over narrowband systems.

Future work will focus on collecting wider-band data from the system, methods of coping with the mutual coupling between the antenna elements, and imaging more realistic biological phantoms.

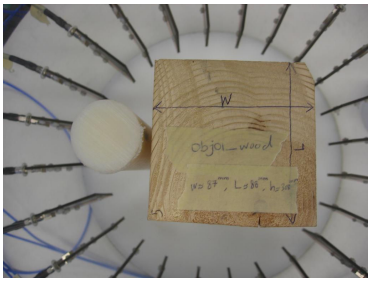

Fig. 4. Dielectric phantom target consisting of teflon and wooden cylinders.

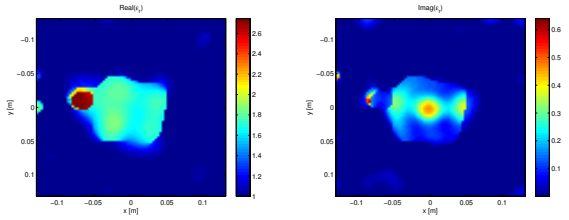

(a) MR-CSI 3 GHz: $Re(\epsilon_r)$ (b) MR-CSI 3 GHz: $-Im(\epsilon_r)$

Fig. 5. MR-CSI reconstruction of the dielectric phantom at 3 GHz.

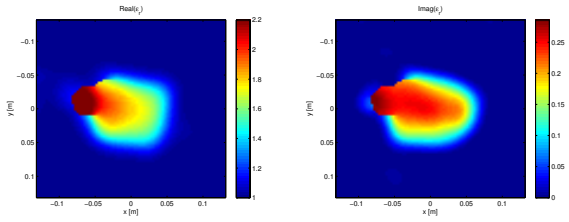

(a) MR-CSI 3-6 GHz: $Re(\epsilon_r)$ (b) MR-CSI 3-6 GHz: $-Im(\epsilon_r)$

Fig. 6. MR-CSI reconstruction of the dielectric phantom using a simultaneous frequency reconstruction from 3-6 GHz (1 GHz steps).

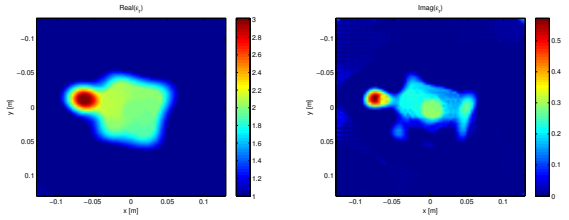

(a) DBIM 3 GHz: $Re(\epsilon_r)$ (b) DBIM 3 GHz: $-Im(\epsilon_r)$

Fig. 7. Enhanced-DBIM reconstruction of the dielectric phantom at 3 GHz.

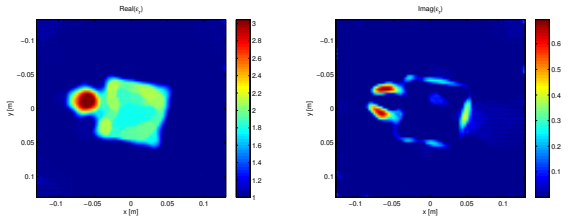

(a) DBIM 3-6 GHz: $Re(\epsilon_r)$ (b) DBIM 3-6 GHz: $-Im(\epsilon_r)$

Fig. 8. Enhanced-DBIM reconstruction of the dielectric phantom using a frequency-hopping reconstruction from 3-6 GHz (1 GHz steps).

REFERENCES

[1] P. M. Meaney, M. W. Fanning, T. Raynolds, C. J. Fox, Q. Fang, C. A. Kogel, S. P. Poplack, and K. D. Paulsen, "Initial clinical experience with microwave breast imaging in women with normal mammography," *Acadademci Radiology*, vol. 14, pp. 207–218, 2007.

[2] S. Semenov, A. Bulyshev, A. Abubakar, V. Posukh, Y. Sizov, A. Souvorov, P. van den Berg, and T. Williams, "Microwave-tomographic imaging of the high dielectric-contrast objects using different image-reconstruction approaches," *Microwave Theory and Techniques, IEEE Transactions on*, vol. 53, no. 7, pp. 2284–2294, July 2005.

[3] S. Y. Semenov, R. H. Svenson, V. G. Posukh, A. G. Nazarov, Y. E. Sizov, A. E. Bulyshev, A. E. Souvorov, W. Chen, J. Kasell, and G. P. Tastis, "Dielectrical spectroscopy of canine myocardium during acute ischemia and hypoxia at frequency spectrum from 100 khz to 6 ghz," *IEEE Trans. Med. Imag*, vol. 21, no. 6, pp. 703–707, June 2002.

[4] Z. Q. Zhang and Q. H. Liu, "Three-dimensional nonlinear image reconstruction for microwave biomedical imaging," *IEEE Trans. Biomed Eng.*, vol. 51, no. 3, pp. 544–548, March 2004.

[5] A. Fhager, P. Hashemzadeh, and M. Persson, "Reconstruction quality and spectral content of an electromagnetic time-domain inversion algorithm," *Biomedical Engineering, IEEE Transactions on*, vol. 53, no. 8, pp. 1594–1604, Aug. 2006.

[6] P. Meaney, M. Fanning, D. Li, S. Poplack, and K. Paulsen, "A clinical prototype for active microwave imaging of the breast," *Microwave Theory and Techniques, IEEE Transactions on*, vol. 48, no. 11, pp. 1841–1853, Nov 2000.

[7] A. Abbosh, H. Kan, and M. Bialkowski, "Compact ultra-wideband planar tapered slot antenna for use in a microwave imaging system," *Microwave Opt Technol Lett*, vol. 48, pp. 2212–2216, 2006.

[8] M. Ostadrahimi, S. Noghanian, and L. Shafai, "A modified double layer tapered slot antenna with improved cross polarization," *13th International Symposium on Antenna Technology and Applied Electromagnetics (ANTEM), Banff, Alberta, Canada, February 15-18*, 2009.

[9] C. Gilmore, A. Abubakar, W. Hu, T. Habashy, and P. van den Berg, "Microwave biomedical data inversion using the finite-difference contrast source inversion method," *Antennas and Propagation, IEEE Transactions on*, vol. 57, no. 5, pp. 1528–1538, May 2009.

[10] C. Gilmore, P. Mojabi, and J. LoVetri, "Comparison of an enhanced distorted born iterative method and the multiplicative-regularized contrast source inversion method," *(To appear) IEEE Transactions on Antennas and Propagation*, 2009.

[11] A. Abubakar, P. M. van den Berg, and J. J. Mallorqui, "Imaging of biomedical data using a multiplicative regularized contrast source inversion method," *IEEE Trans. Microwave Theory Tech.*, vol. 50, no. 7, pp. 1761–1777, July 2002.

[12] P. M. van den Berg and R. E. Kleinman, "A contrast source inversion method," *Inverse Probl.*, vol. 13, pp. 1607–1620, 1997.

[13] W. C. Chew and Y. M. Wang, "Reconstruction of two-dimensional permittivity distribution using the distorted born iterative method," *IEEE Trans. Med. Imaging*, vol. 9, no. 2, pp. 218–225, 1990.

[14] J. D. Zaeytijd, A. Franchois, C. Eyraud, and J. Geffrin, "Full-wave three-dimensional microwave imaging with a regularized Gauss-Newton method–theory and experiment," *IEEE Trans. Antennas Propag.*, vol. 55, no. 11, pp. 3279–3292, Nov 2007.

[15] P. van den Berg, A. Abubakar, and J. Fokkema, "Multiplicative regularization for contrast profile inversion," *Radio Science*, vol. 38, pp. 23.1–23.10, 2003.